Journal of The Electrochemical Society, **154** (4) B419-B426 (2007)
0013-4651/2007/154(4)/B419/8/$20.00 © The Electrochemical Society

Modeling of Two-Phase Behavior in the Gas Diffusion Medium of PEFCs via Full Morphology Approach

Volker Paul Schulz,[a,z] Jürgen Becker,[a] Andreas Wiegmann,[a] Partha P. Mukherjee,[b,*] and Chao-Yang Wang[b,]**

[a]*Fraunhofer-Institut für Techno- und Wirtschaftsmathematik (ITWM), Kaiserslautern, Germany*
[b]*Electrochemical Engine Center (ECEC), and Department of Mechanical and Nuclear Engineering, The Pennsylvania State University, University Park, PA 16802, USA*

A full morphology (FM) model has been developed for studying the two-phase characteristics of the gas diffusion medium in a polymer electrolyte fuel cell (PEFC). The three-dimensional (3D) fibrous microstructure for the nonwoven gas diffusion layer (GDL) microstructure has been reconstructed using a stochastic technique for Toray090 and SGL10BA carbon papers. The FM model directly solves for the capillary pressure-saturation relations on the detailed morphology of the reconstructed GDL from drainage simulations. The estimated capillary pressure-saturation curves can be used as valuable inputs to macroscopic two-phase models. Additionally, 3D visualization of the water distribution in the gas diffusion medium suggests that only a small number of pores are occupied by liquid water at breakthrough. Based on a reduced compression model, the two-phase behavior of the GDL under mechanical load is also investigated and the capillary pressure-saturation relations are evaluated for different compression levels.
 [DOI: 10.1149/1.2472547]

Manuscript submitted July 11, 2006; revised manuscript received December 13, 2006. Available electronically February 21, 2007.

The polymer electrolyte fuel cells (PEFCs), which convert the chemical energy of hydrogen directly into electrical energy, are considered as the most promising alternative energy-conversion devices in the 21st century for several applications including automotive, stationary and portable power. The electrochemical reaction occurring in the cathode catalyst layer (CL), referred to as the oxygen reduction reaction combines protons, resulting from hydrogen oxidation in the anode catalyst layer, with oxygen to produce water and waste heat. Although tremendous progress has been made in recent years in enhancing overall performance of the PEFC, one major performance-limiting step is the coverage of the reaction sites in the CLs as well as the blockage of the reactant-transporting networks in the porous gas diffusion layers (GDLs) due to liquid water, which hinders the oxidant from reaching the active reaction sites in the CLs at high current density operation. The GDL plays a crucial role in the overall water management which requires a delicate balance between reactant transport from the gas channels and water removal from the electrochemically active sites. Mathias et al.[1] provided a comprehensive overview of GDL structure and functions.

Several studies have been attempted in recent years to model two-phase behavior and flooding phenomena in polymer electrolyte fuel cells in various degrees of complexities.[2-15] Recent reviews by Wang[16] and Weber and Newman[17] provide comprehensive overview of various two-phase PEFC models and address the water management issue with particular attention to GDL in significant details. However, all of the above-mentioned macroscopic two-phase models are plagued with the scarcity of realistic two-phase correlations, in terms of capillary pressure and relative permeability as functions of water saturation, tailored specifically for actual gas diffusion medium characterized by woven or nonwoven fibrous structures. Due to the lack of reliable two phase correlations, these models often deploy a generic curve-fitted capillary pressure-saturation data originally obtained by Udell[18] in the form of Leverett-J function from imbibition in water-wet unconsolidated sand.[19] In order to enhance the fidelity of the two-phase computational fuel cell dynamics models, it is imperative to investigate the interplay between underlying microstructure and two-phase characteristics of the porous gas diffusion medium in polymer electrolyte fuel cells.

Recently, Gostick et al.[20] reported capillary pressure-saturation data for various GDL materials from drainage experiments using standard porosimetry technique. However, hardly any modeling efforts in estimating two-phase characteristics of the GDL in terms of capillary pressure as a function of liquid water saturation have been reported in the literature.

In the present study, digital computer models of nonwoven carbon paper GDLs are reconstructed using a stochastic generation method[21,22] with structural inputs, namely fiber diameter, fiber orientation, and porosity, obtained from two-dimensional scanning electron microscopy (SEM) micrographs of the GDL and related available data from literature. A full morphology (FM) model[23-25] is subsequently developed, which is again the attempt to investigate two-phase behavior in the reconstructed GDL microstructures by simulating a drainage process. Capillary pressure as function of liquid water saturation is estimated for two different nonwoven GDL materials. The capillary pressure correlations predicted by the FM model are subsequently compared with experimental data available in the literature.[20] Furthermore, the effect of cell clamping pressure on the two-phase characteristics of a carbon paper GDL is investigated. The importance of clamping pressure on fuel cell performance has been studied by several researchers. Notable works include Mathias et al.,[1] Wilde et al.,[26] and Ihonen et al..[27] Mathias et al.[1] reported compression and flexural behavior of carbon paper and carbon cloth GDLs and indicated the effect of compressive characteristics on the channel flow-field pressure drop. Wilde et al.[26] studied the impact of compression force on the GDL properties, namely electrical resistivity, pore size, and permeability for different materials and briefly described the resulting influence on PEFC performance. Ihonen and co-workers,[27] on the other hand, tried to assess experimentally the influence of clamping pressure on the flooding behavior of the GDL. However, none of these studies focused on the dependency of capillary pressure-saturation relation on clamping pressure through its tight coupling on the underlying GDL structure. In the present study, we report the variation of two-phase correlations in terms of capillary pressure-water saturation relation for the GDL with various levels of cell compression. Finally, the predictive capability of the present model in estimating realistic two-phase correlations for input into macroscopic two-phase fuel cell dynamics models is emphasized.

Experimental

The construction of a realistic GDL pore morphology is the essential prerequisite for unveiling the influence of the underlying structure on the two-phase behavior. This can be achieved either by three-dimensional (3D) volume imaging or by constructing a digital microstructure based on stochastic models. Noninvasive experimental techniques, such as X-ray and magnetic resonance computed

* Electrochemical Society Student Member.
** Electrochemical Society Active Member.
z E-mail: volker.schulz@itwm.fraunhofer.de

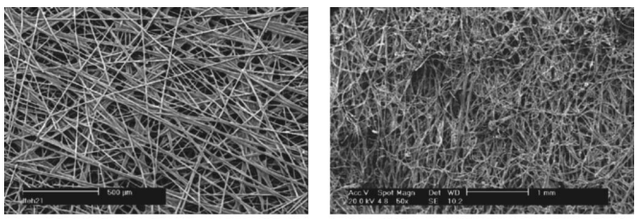

(a) (b)

Figure 1. SEM surface images of the investigated carbon papers. (a) A Toray090 with 30 wt % polytetrafluoroethylene and (b) SGL10BA.

microtomography are the popular methods for the 3D imaging of the pore structure. Another alternative is the reconstruction of the microstructure using stochastic simulation techniques. The low cost and high speed of data generation make the stochastic generation methods the preferred choice over the experimental imaging techniques. In the present study, the GDL is a nonwoven carbon paper, which consists of well-defined carbon fibers with a fixed diameter. As can be observed from the SEM micrograph image of a typical carbon paper GDL in Fig. 1, the fibers are randomLy oriented in the *xy* plane, which leads to an anisotropic material characterized by in-plane and through-plane properties.

In order to develop a manageable model for the microstructure generation, the following assumptions are particularly made about the investigated carbon-paper GDLs:

The fibers are long compared to the sample size and their crimp is negligible.

The interaction between the fibers can be neglected, i.e., the fibers are allowed to overlap.

Due to the fabrication process, the fiber system is macroscopically homogeneous and isotropic in the material plane, defined as the *xy* plane. This implies that the distribution properties of the stochastic model are invariant with respect to translations as well as rotations about the *z* axis.

These assumptions justify a stationary Poisson line process with a one-parametric directional distribution, where the cylinders are attached to the centers of the lines. The diameter and shape distribution can be selected according to the specifications provided by the manufacturer of the nonwoven carbon paper GDL. In the current work, we restrict ourselves to circular cross sections typical for carbon fibers. Following the approach in Ref. 22, the directional distribution is given in polar coordinates by its density. Thus, the density $p(\theta,\varphi)$ is chosen as a function of the altitude θ and the longitude φ

$$p(\theta,\varphi) = \frac{1}{4\pi}\frac{\beta \sin\theta}{(1 + (\beta^2 - 1)\cos^2\theta)^{\frac{3}{2}}} \quad [1]$$

Due to the isotropy in the *xy* plane, $p(\theta,\varphi)$ is independent of φ. We call β the anisotropy parameter where the case $\beta = 1$ describes an isotropic cylinder system. For increasing β the fibers tend to be more and more parallel to the *xy* plane.

Microstructural characterization.— Using the input parameters given in Table I, the microstructures of a Toray090 and a SGL10BA carbon paper GDL are reconstructed. Apart from having lower porosity as compared to the SGL10BA GDL, in the Toray090 carbon paper the fibers are fixed by a resin binder[1] while its amount can vary significantly. Additionally, there is a significant difference between the two investigated materials since the fiber orientation of the Toray090 is strongly anisotropic. The fiber orientation of the stochastic microstructure generation is reflected by the anisotropy factor β, Eq. 1. In this sense, β has to be large enough in order to suppress fibers which are oriented along the *z* axis.[28] In our simulation, we have chosen a value of $\beta = 10{,}000$. The smaller value of $\beta = 100$ for the reconstruction of a SGL10BA (see Table I) corresponds to a smaller anisotropy of the material compared to the Toray090. In the context of the current work, the structure generation model is further validated in terms of the permeability of the digital microstructure with the available experimental data in the literature. But we note that there is a great potential to improve the structure generation, e.g., the simulation of crimped fibers, which can be seen as an extension of the approach presented in this paper.

Nevertheless, due to the material properties the binder is a wetting fluid with respect to the carbon fibers and its distribution follows the capillary forces. As a consequence the binder fills the small pores, i.e., all regions where the fibers are close packed already. An entire study of the relation between binder amount and the GDL properties is beyond the scope of this work. However, it can be safely assumed that the impact of the binder amount is rather small in the range of low nonwetting phase distribution. This is especially true for a highly porous and therefore a highly connected pore space. The 3D, reconstructed microstructures of the Toray090 and SGL10BA GDLs are shown in Fig. 2.

Additionally, Fig. 3 exhibits the virtual SEM-like images from the reconstructed Toray090 and SGL10BA carbon paper GDLs, respectively, and they demonstrate good correspondence with the actual SEM images. As one can see from the comparison of Figs. 3b and 1b, neglecting the crimp of the fibers is a relatively strong simplification for the SGL10BA while the overall statistical parameters are still captured as shown in the following sections.

The structural properties, namely pore size distribution and intrinsic permeability of the GDL microstructures, are evaluated in order to validate these digital models against the physical properties of the real carbon paper GDLs.

Pore size distribution from granulometry.— The morphological opening with spheres of increasing radius is employed in order to determine the pore size distribution of the 3D microstructures.[29] Figures 4 and 5 show the pore size distributions for the reconstructed Toray090 and SGL10BA carbon paper GDLs, respectively, which are in good agreement with the measured data. Gostick et al.[20] report a mean pore radius of Toray090 in the range of 9–12 μm.

Permeability.— The permeability tensor k is the proportionality constant between the average fluid velocity and applied pressure gradient in the porous medium. For the determination of k we performed a numerical micropermeatry on the 3D fiber structure by solving appropriate Stokes equation at low Reynolds numbers in the pore space using the lattice-Boltzmann (LB) method.[30-32] An attractive feature of the LB method is its ability to handle boundary conditions in any geometric structure with small numeric effort. To get correct no-slip boundary conditions for arbitrary viscosities, we apply the multirelaxation scheme (generalized lattice Boltzmann

Table I. Parameters used for the reconstruction of the investigated materials. The parameter β is a measure of the anisotropy of the fibers and defined in Eq. 1.

	Length/Width		Thickness		Fiber diameter	Porosity	β
Material	(voxel)	(mm)	(voxel)	(μm)	(μm)	(–)	(–)
Toray090	2048	1.52	256	190	7	0.78	10,000
SGL10BA	2048	3.04	256	380	7	0.88	100

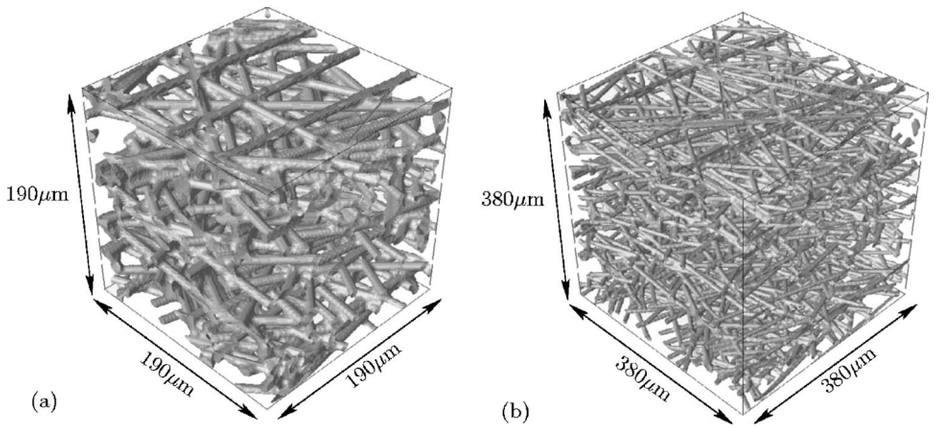

Figure 2. Visualized cutout of the reconstructed (a) Toray090 and (b) SGL10BA.

method).[33,34] For a given pressure gradient, ∇P, the velocity field and the average velocity υ through the system in the stationary state is calculated and thereafter the permeability, k, is evaluated using Darcy's law

$$\upsilon = -\frac{k}{\mu}\nabla P \qquad [2]$$

where μ is the dynamic viscosity of the fluid. The permeability, k, in Darcy's law (Eq. 2) does not depend on the fluid and is a pure geometric property measured in darcy (1 darcy $\simeq 10^{-12}$ m^2).

Table II shows that for both Toray090 and SGL10BA diffusion media the difference between the simulated permeability and measured data is in the range of 10–15%. For the simulation we used a cutout of 512 × 512 × 256 voxels. Since this deviation is in the order of macroscopic heterogeneities of the material, i.e., variation of the porosity, we conclude that a realization of the microstructure representative of the essential geometric features of the real nonwoven material is achieved.

Full-morphology model: Capillary pressure-saturation relation.— Once the three-dimensional microstructure of the gas diffusion medium is generated, the stationary distribution of the wetting and nonwetting phases for arbitrary capillary pressure, p_c, can be evaluated using a so-called full-morphology (FM) approach, which simulates the drainage process through the initially wetting phase saturated GDL. The FM approach is based on the original works by Hazlett[23] and Hilpert and Miller[24] and was compared to Lattice-Boltzmann and pore network models in Ref. 25.

In the present work, the FM model is systematically employed for the quasi-static drainage simulation of liquid water within the nonwoven GDL and the model development relies on our preliminary work in Ref. 35.

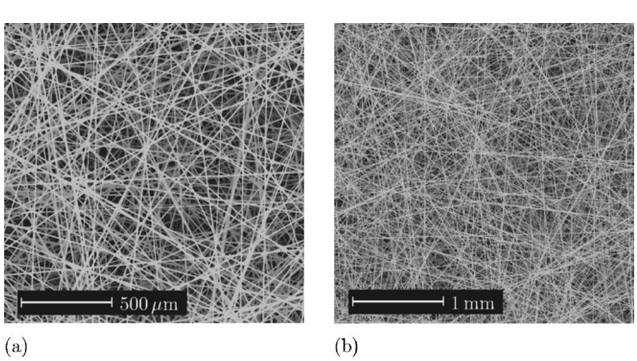

Figure 3. Visualization similar to a SEM image of the reconstructed Toray090 (a) and SGL10BA (b), respectively.

Model description.— In order to determine the pore space that will be accessible for the nonwetting phase (NWP) at a given pressure during drainage, the image is decomposed with the pore radius as ordering parameter. This can be done by a morphological opening which is defined as

$$\mathcal{O}_B(X) = \cup \{B | B \subseteq X\} \qquad [3]$$

In this case, X represents the pore space and B is a structuring element. In other words, the morphological opening determines the part of the pore space where the structuring element fits in. With the choice of the structuring element B, we make an assumption about the form of the interphase between $\mathcal{O}_B(X)$ which is associated with the NWP and $X - \mathcal{O}_B(X)$ associated with the WP. A common choice is spheres with different radii implying a spherical interphase between the two phases which is a reasonable approximation for isotropic porous media.

For a three-dimensional image of the structure, the opening with spherical structuring elements B_r with different radii $r \in [0, r_{\max}]$ can be used to get a size distribution since it fulfills the relation

$$\mathcal{O}_{B_{r'}} \subset \mathcal{O}_{B_r} \quad \forall\, r' > r \qquad [4]$$

This corresponds to the concept of a granulometry[29] and has been successfully applied to porous media.[24,36] For $r = 0$, $\mathcal{O}_{B_r}$ measures the total pore space, and $r_{\max}$ corresponds to the radius of the

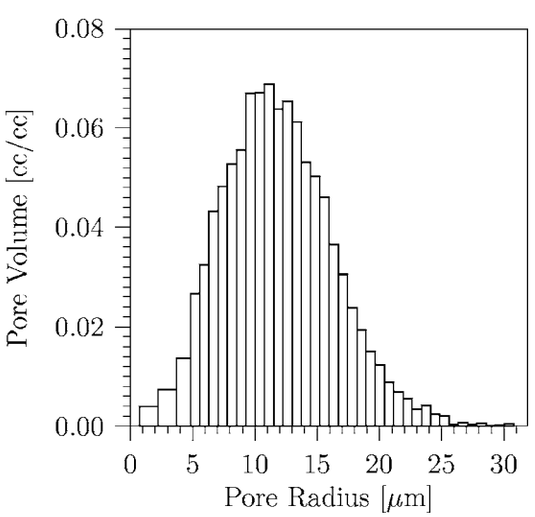

Figure 4. Pore size distribution of the reconstructed Toray090. For small pore radii the data were merged to reduce numerical artifacts due to the voxelized image.

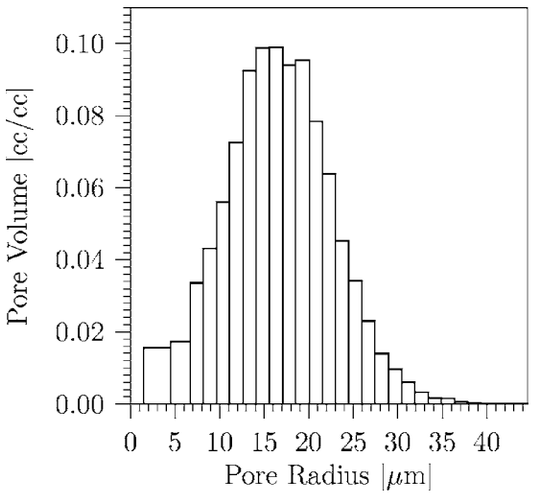

Figure 5. Pore size distribution of the reconstructed SGL10BA.

maximum sphere that fits in the pores space at any point. Within these upper and lower bounds, r measures the constant curvature radius of the WP-NWP interface and herewith can be associated with a capillary pressure.

The pertinent steps of the approach for the determination of the quasi-static primary drainage curve $s_w(p_c)$ are as follows:

1. Initially, the entire pore space is filled with WP and the capillary pressure is zero. At one end, the diffusion medium is connected to a NWP reservoir while at the opposite end it is connected to the WP reservoir.

2. The pore space X is eroded by spheres with increasing radius r starting with the smallest radius, i.e., $r = 1$. The erosion is defined as

$$\varepsilon_{B_r}(X) = \{x:B_{x,r} \subseteq X\} \quad [5]$$

where $B_{x,r}$ is the structuring element centered at point x. We identify the radius r with the corresponding pressure according to the Young-Laplace equation

$$p_c = \frac{2\gamma \cos\theta}{r} \quad [6]$$

where γ is the surface tension between NWP and WP and θ the contact angle between WP and solid.

3. At the given capillary pressure, pores can be filled with NWP only if the erosion of the pore space has a continuous connection to the nonwetting reservoir. Hence, all pores are removed from the eroded pore space which are separated from this reservoir.

4. To determine the phase saturations, s_n and s_w for the NWP and WP, respectively, related to the given capillary pressure p_c, the eroded set is dilated using the same structuring element as for erosion

$$\mathcal{D}_{B_r}[\boldsymbol{\varepsilon}_{B_r}(\boldsymbol{X})] = \{\boldsymbol{x}:\boldsymbol{B}_{x,r} \cap \boldsymbol{\varepsilon}_{B_r}(\boldsymbol{X}) \neq \emptyset\} \quad [7]$$

It finally leads to the opening $\mathcal{O}_{B_r}(X)$ of the pore space with respect to B_r as defined in Eq. 3. Then s_n is simply the volume fraction of $\mathcal{O}_{B_r}(X)$ related to the total pore volume and $s_w = 1 - s_n$.

5. We proceed with step 2 for the next pressure step using the next larger structuring element.

In contrast to earlier publications in the framework of the FM model, our algorithm is not directly based on a structuring element. We take advantage of the fact that both the morphological erosion and the morphological dilation with spheres can be expressed by the parallel body of the structure.[37] Thus, the erosion and the dilation of the binary structure reduce to the problem of computing the euclidian distance map which has been solved already in a very smart way by Saito and Toriwaki.[38] It is worth noting that the application of the FM model is particularly suitable for the simulation of two-phase behavior within the GDL of a PEFC which exhibits only a small fraction of the pore space being occupied with liquid water under typical operating conditions.

Results and Discussions

Numerical experiment of primary drainage.— The basic idea of the numerical drainage experiment is to calculate the quasi-static states for the distribution of the wetting phase (WP) and the nonwetting phase (NWP) in the 3D porous sample. Initially the entire pore space of the GDL microstructure is filled with the wetting phase. The GDL sample is connected to a wetting-phase reservoir and a nonwetting phase reservoir at opposite ends in the flow direction. All other sides are closed. It is to be noted that for a hydrophobic GDL, air is the wetting phase and water is the nonwetting phase in a drainage experiment. To simulate the primary drainage process, we start with zero capillary pressure by applying a constant pressure of equal magnitude at both the reservoirs. Subsequently, the pressure difference between the wetting phase and the nonwetting phase reservoirs is reduced stepwise leading to increased capillary pressures. As a result, the pores are filled if they are "large" enough and have a connection to the NWP reservoir.

Thus, in the current simulation the bubble point can be exactly defined as the first continuous path for a sphere with radius, r, connecting two opposite ends of the porous sample.

Numerical experiment of the saturation for arbitrarily mobile fluids.— The requirement of a connection to the NWP reservoir is essential in the drainage simulation. Thus, not only the pore size distribution but also the connectivity of the pores plays an important role in the capillary pressure-saturation characteristics. When the connectivity of the pores to the reservoir is neglected the algorithm can be used to determine the cumulative pore size distribution. With

Table II. Permeabilities of the microstructures as determined by Lattice-Boltzmann flow simulations. The sample size was 512 × 512 × 256 voxels.

	In plane		Through plane		In plane/through plane	
Material	Simulation (10^{-12} m^2)	Measured (10^{-12} m^2)	Simulation (10^{-12} m^2)	Measured)10^{-12} m^2)	Simulation (–)	Measure (–)
Toray090	11.5	…[a]	7.4	8.3[b]	1.55	–[a]
SGL10BA	30.9	33[c]	21.1	18[c]	1.46	1.83[c]

[a] No published data available.
[b] Reference 20.
[c] Reference 27.

the aid of the Young–Laplace's equation, Eq. 6, the cumulative pore size distribution can be interpreted as a capillary pressure-saturation curve. From a physical point of view this corresponds to phase distributions due to arbitrarily mobile wetting and nonwetting fluids. Neglecting the connectivity of the pores corresponds to a bundle of capillaries and can be seen as a lower bound of the capillary pressure-saturation curve.[39]

Capillary pressure-saturation curves.— The selection of an appropriate contact angle is the key to the quantitative evaluation of capillary pressure-saturation relation, as is evident from the Young–Laplace's equation, Eq. 6. However, there is wide debate over the actual contact angle of the GDL materials reported in the literature. For instance, Benziger et al.[40] reported a measured contact angle for the Toray090 carbon paper of 170° for the advancing water and 120° for the receding water, respectively. Please note that it is common practice to define the contact angle with respect to the water regardless if water is the nonwetting or the wetting fluid. Thus, a contact angle larger than 90° indicates that the material is hydrophobic.

Additionally, it is often assumed that the contact angle does not vary with Teflon amounts in the range of 20–60%. In contrast, Gostick et al.[20] distinguished between an observed and an effective contact angle and reported values of 146° and 112°, respectively. Investigations by Mathias et al.[1] showed the influence of the technique on the measured contact angle. For the slightly thinner Toray060, they found values between 135° and 156° depending on the Teflon amount by the sessile drop method. Using the Wilhelmy method, they determined values between 170° for advancing and 134° for receding water. Benziger et al.[40] measured the capillary pressure at the bubble point of the material in the range of 0.05–0.1 bar. From the FM model we determine a pore radius of 10.39 μm at the bubble point. This is in agreement with the data from Benziger et al.[40] when we assume a contact angle between 111° and 136°. Therefore, in the present study, we use an average contact angle of 120° for our predictions.

It is important to note that since the quasi-static two-phase distribution in the FM model is based on a purely morphological consideration of overlapping spheres, the static contact angle of 120° deployed in the Young–Laplace equation, Eq. 6, rather acts as a numerical parameter in the evaluation of the capillary pressure and, however, does not reflect in the corresponding interfacial shape between the two phases. The influence of the contact angle on the shape of the geometrical fitting element instead of a spherical element in the two-phase distribution is envisioned as a future extension of the current FM model.

Figure 6 shows the capillary pressure-NWP saturation relations for the Toray090 and the SGL10BA GDL from the primary drainage as well as the simulations based on arbitrarily mobile fluids. It is to be noted that the GDL sample size for the drainage simulation is chosen to be 2048 × 2048 × 256 voxels as mentioned in Table I.

Both the Toray090 and SGL10BA GDL microstructures exhibit similar entry pressure for the initiation of the invasion of the nonwetting phase into the wetting phase saturated domain in the primary drainage experiment. As expected, both the GDL structures display close agreement between the capillary pressure curves predicted by the primary drainage simulation and the assumption of arbitrarily mobile fluids toward the irreducible saturation limit. The Toray090 GDL exhibits gradual increase of capillary pressure in the liquid water saturation level ranging between 0.1 and 0.6. The SGL10BA GDL, on the other hand, shows a sudden jump in the liquid water saturation level from 0.1 to 0.6 with negligible increase in the capillary pressure. These observations are direct manifestations of the underlying pore morphology and such capillary pressure-saturation relations could prove to be valuable inputs for macroscopic two-phase fuel cell models.

Nonwetting phase distribution in the drainage process.— Figure 7 shows the static liquid water saturation distributions within the Toray090 GDL microstructure at different capillary pressure levels obtained from the primary drainage experiment. At bubble point, the

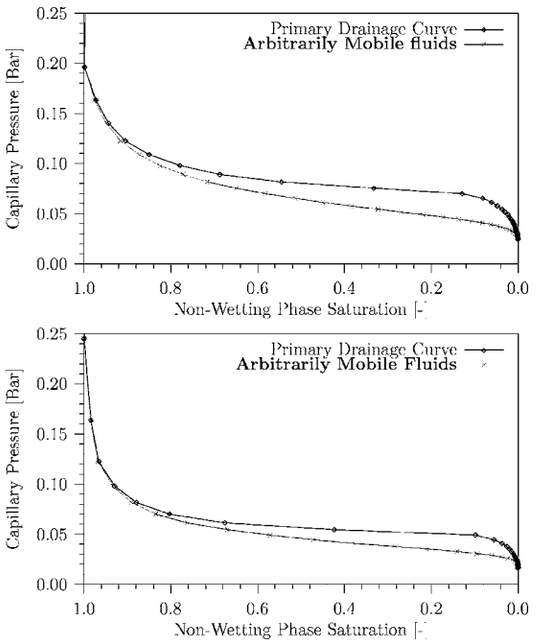

Figure 6. Capillary pressure-saturation curves determined by the full morphology model. Shown is the primary drainage curve where the nonwetting phase enters the sample from the top or bottom of the sample. In the case of the arbitrarily mobile fluids, the connectivity of the pores is neglected. The contact angle was set to 120°. Top: Toray090, bottom: SGL10BA.

invading liquid water front finds a connected pathway through the GDL structure and reaches the air reservoir. From the saturation distribution observed at the bubble point state, it is clear that with increasing capillary pressure, several water fronts start penetrating into the air-saturated domain based on the pore size distribution and the resulting capillary force in the pattern of fractal fingering. This pattern of the liquid water saturation predicted under infinitesimal capillary number cannot be compared with the liquid water saturation map observed by Djilali and co-workers[41,42] in ex situ experiments by injecting 0.02 mL/min liquid water into a 0.0314 cm^2 GDL area which corresponds to an equivalent current density of 112 A/cm^2.

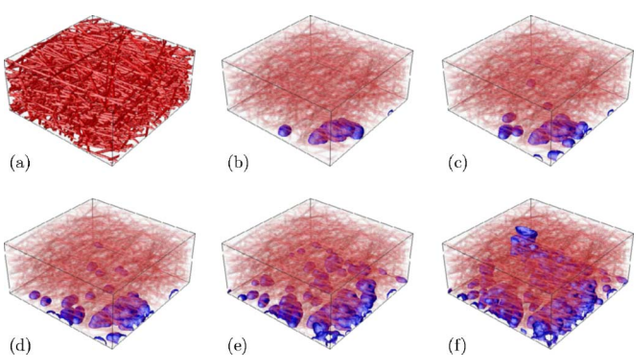

Figure 7. (Color online) Visualization of the nonwetting phase distribution in the simulated drainage process as iso surface plots. In (a), the void space is entirely filled with the wetting phase. The images (b)–(f) show the quasi-static states of the penetrating nonwetting phase with increasing capillary pressure. The nonwetting phase enters the pores from the bottom. In (f) the bubble point is reached which corresponds to a connecting path from the bottom to the top.

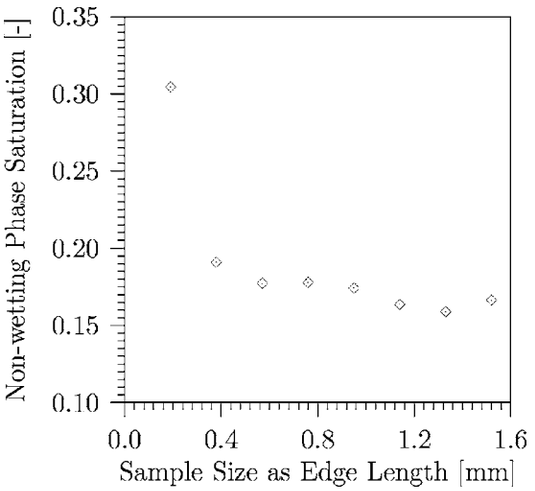

Figure 8. Impact of the sample size on the nonwetting phase saturation of the simulated Toray090 at the bubble point. For all sizes the capillary pressure at the bubble point is 0.1 bar.

Effect of the sample size on the nonwetting phase saturation.— Compared to other simulation techniques, the FM model allows the investigation of rather large sample sizes. But compared to the macroscopic flow field in the GDL the dimensions are still small and one has to take care of the size effects. This is especially the case for the saturation near the bubble point which is important from the actual fuel cell operation standpoint. For a random heterogeneous medium, such as the investigated carbon papers, the saturation in the drainage process depends on the pore size distribution and the connectivity of the pores. In particular the connectivity of the pores can exhibit large variations for small samples. The impact of the sample size for a Toray090 GDL microstructure on the water saturation is shown in Fig. 8 where the bubble point saturation for increasing sample sizes is shown. As can be seen from Fig. 8, the water saturation varies between 0.15 and 0.31 for different sample sizes. The large difference at small sample size is expected but it is remarkable that even on a mm scale, variation of about 10% can be found. However, the percolation threshold and the corresponding capillary pressure using the Young-Laplace's law are not affected by the sample size.

Leverett-J function.— Figure 9 shows the capillary pressure-saturation data in terms of Leverett-J function for the Toray090 and SGL10BA GDLs from the drainage simulations along with measured data reported by Gostick et al.[20] The J-function curves for both the GDLs exhibit a similar trend. Toray090 GDL displays very good agreement with the measured data over the entire saturation

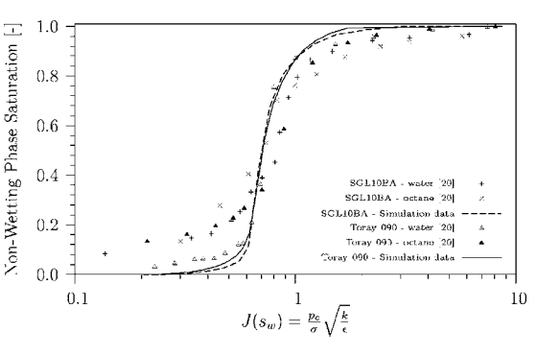

Figure 9. Leverett-J function of the investigated material in comparison to published measured data from Gostick et al.[20]

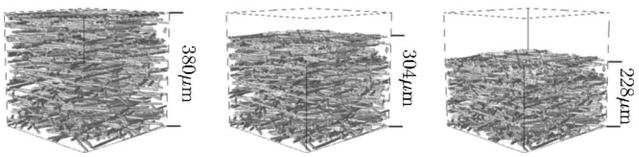

Figure 10. Cutout of the virtually compressed SGL10BA. The compression ratio from the left to the right is 1.0, 0.8, and 0.6.

range while the SGL10BA GDL shows reasonable agreement with the experimental measurements especially in the higher saturation range. However, it should be noted that the J function reported by Gostick et al.[20] does not include the contact angle effect on the capillary pressure-saturation behavior.

Effect of clamping pressure.— Compression modeling.— The detailed modeling of a porous material under compression is a challenging task of applied structural mechanics. In the context of the current work, a reduced model of compression is employed. The present model is based on a macroscopically homogeneous material which is fixed at one end (bottom) and loaded on the opposite end (top). Thus, the displacement is zero at the bottom and maximal at the top of the sample. Neglecting the transverse strain, we can directly transfer that macroscopic behavior into a displacement of the solid voxels. The compression ratio, c, is defined as

$$c = \frac{\text{Height of the compressed sample}}{\text{Initial height}} \quad [8]$$

The new height h' of each voxel can be calculated as its position along the z axis by

$$h' = [ch] \quad [9]$$

where h is the uncompressed position and the square brackets indicate rounding to the closest integer. Additionally, in the reduced compression model, we do not allow the solid voxels to penetrate into each other. Thus, with increasing compaction ratio more voxels lay on top of each other since the x-y position is maintained fixed. However, with our reduced model, it is difficult to find a relation between the compression ratio and the external load. Nevertheless, our approach leads to reliable 3D morphology of the nonwoven GDL structures under compression and is detailed in the next section.

Through-plane permeability under compression.— The compression model was applied to the reconstructed SGL10BA GDL microstructure in order to realize compression ratios of 0.9, 0.8, 0.7, 0.6, and 0.5. The compression ratios of 0.8 and 0.6 are shown in Fig. 10 together with the uncompressed sample (compression ratio equals 1).

For the five compression ratios, the permeability was determined in the through-plane direction using the lattice-Boltzmann model. These values were normalized with respect to the permeability of the uncompressed sample of 21.1 of darcy as reported in Table II, and are shown in Fig. 11. Dohle et al.[43] published measured data of the through-plane permeability of a SGL10BA for different compression ratios. These data are included in Fig. 11 and show a similar trend as our simulation. Due to the limited data available in the context of this work it is not possible to give a quantitative evaluation of the reduced compression model.

Variation of the pore size distribution under compression.— Due to the compression of the sample, the pore size distribution is expected to shift toward smaller pores. Figure 12 shows the pore size distributions of the uncompressed and 50% compressed GDL microstructures. It can be observed that the maxima of the pore size distribution changes from about 17 to about 10 µm under 50% compression. Interestingly, the width of the distribution is only slightly reduced.

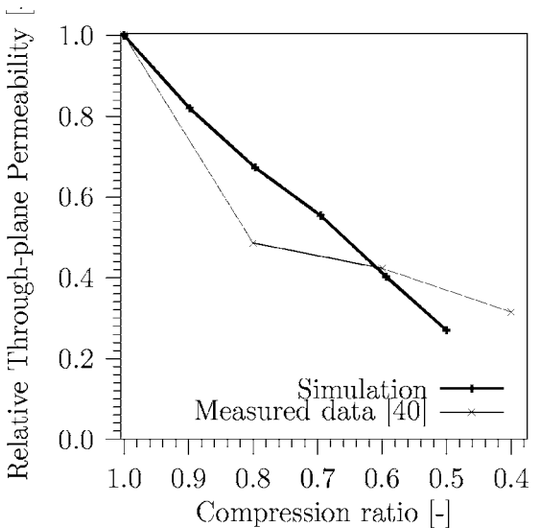

Figure 11. Through-plane permeability normalized to the value of the uncompressed sample versus the compression ratio.

Capillary pressure-saturation curves.— The primary drainage simulation was performed using the FM model with the uncompressed and compressed SGL10BA GDL microstructures. The variation of nonwetting phase saturation with capillary pressure is shown in Fig. 13 for the SGL10BA GDL in the uncompressed state as well as with compression ratio of 0.7 and 0.5 from the primary drainage simulation.

It is quite evident that increased compression leads to more tortuous pore structure which in turn requires increasing capillary pressure for the invasion of the nonwetting phase into the wetting phase saturated GDL in order to achieve the same level of saturation. The increase in the bubble point pressure with increased compression level further testifies the extra level of resistance offered by the compressed GDL owing to the underlying morphology as opposed to the uncompressed sample. The capillary pressure-saturation curves are further fitted according to the van Genuchten correlation

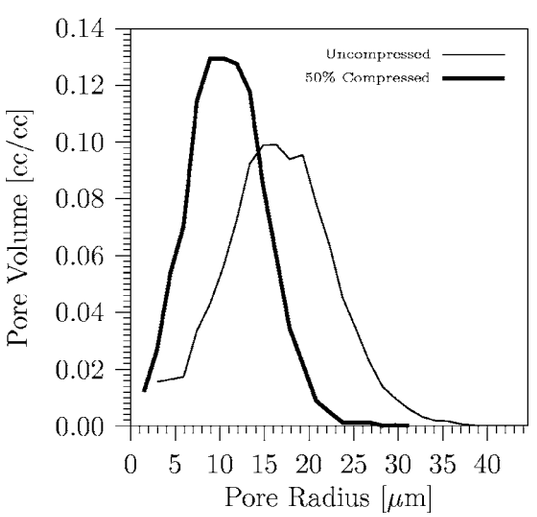

Figure 12. Comparison of the pore size distribution of the uncompressed and the 50% compressed sample. The data of the uncompressed case are equivalent to box plot Fig. 5.

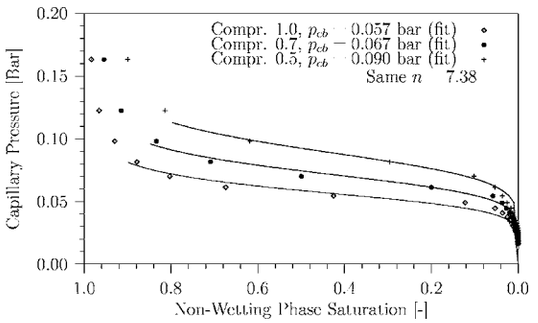

Figure 13. SGL10BA: Capillary pressure-saturation curves for primary drainage for uncompressed and compressed samples. The simulation data can be fitted to a van Genuchten function with the same parameter n for the different compression ratios.

$$p_c(s_w) = p_{cb}(s_w^{-n/(n-1)} - 1)^{1/n} \quad [10]$$

and all the compression levels can be adequately realized with the same parameter, $n = 7.38$. It should be noted that the van Genuchten correlations match particularly well with the simulated data toward the lower bounds of the water saturation range.

Conclusion

The two-phase characteristics in terms of capillary pressure-saturation relation for the Toray090 and SGL10BA GDL materials is evaluated using the FM approach based on the realistic digital microstructures of the investigated nonwoven GDL materials.

The GDL microstructures are realized using a stochastic reconstruction technique and the reconstructed structures exhibit good agreement with the measured microstructural properties. The capillary pressure-saturation data obtained from the simulations can be used as valuable inputs to the macroscopic two-phase fuel cell models as closure relations. The importance of clamping pressure on the two-phase characteristics is demonstrated through the evaluation of capillary pressure curves for various levels of compression through the deployment of a reduced compression model coupled with the FM model for the SGL10BA GDL.

The two-phase characteristic of a compressed GDL is determined based on its full 3D microstructure. Overall the comprehensive modeling capability described in the present work is of significant importance in terms of providing reliable two-phase correlations for high-fidelity two-phase simulations where the GDL compression effect can be adequately described.

Finally, one of the major strengths of our approach lies in its application for virtual material design since we relate the material properties to the underlying 3D microstructure.

Acknowledgments

Thanks are due to J. T. Gostick from the University of Waterloo, Canada, for the experimental Leverett-J function data as well as the SEM image of the SGL10BA carbon paper, F. Q. Liu of ECEC for the Toray090 carbon paper SEM image and P. M. Wilde from SGL Technologies GmbH, Germany, for fruitful discussions on the GDL compression effect. The authors acknowledge financial support for this work from the BMBF-project PEMDesgin (no. 03SF0310A).

References

1. M. Mathias, J. Roth, J. Fleming, and W. Lehnert, in *Handbook of Fuel Cells*, Vol. 3, W. Vielstich, A. Lamm, and H. Gasteiger, Editors, Wiley, New York (2003), .
2. U. Pasaogullari and C. Y. Wang, *J. Electrochem. Soc.*, **151**, A399 (2004).
3. U. Pasaogullari and C. Y. Wang, *Electrochim. Acta*, **49**, 4359 (2004).
4. A. Z. Weber, R. M. Darling, and J. Newman, *J. Electrochem. Soc.*, **151**, A1715 (2004).
5. A. Z. Weber and J. Newman, *J. Electrochem. Soc.*, **152**, 677 (2005).
6. Z. H. Wang, C. Y. Wang, and K. Chen, *J. Power Sources*, **94**, 40 (2001).
7. T. Berning and N. Djilali, *J. Electrochem. Soc.*, **150**, A1589 (2003).
8. M. Noponen, E. Birgersson, J. Ihonen, M. Vynnycky, A. Lundblad, and G. Lindbergh, *Fuel Cells*, **4**, 365 (2004).

9. S. Mazumder and J. Cole, *J. Electrochem. Soc.*, **150**, A1510 (2003).
10. J. Nam and M. Kaviany, *Int. J. Heat Mass Transfer*, **46**, 4595 (2003).
11. G. Lin, W. He, and T. V. Nguyen, *J. Electrochem. Soc.*, **151**, A1999 (2004).
12. D. Natarajan and T. V. Nguyen, *J. Power Sources*, **115**, 66 (2003).
13. D. Natarajan and T. V. Nguyen, *J. Electrochem. Soc.*, **148**, A1324 (2001).
14. W. He, J. S. Yi, and T. V. Nguyen, *AIChE J.*, **46**, 2053 (2000).
15. L. You and H. Liu, *Int. J. Heat Mass Transfer*, **45**, 2277 (2002).
16. C. Y. Wang, *Chem. Rev. (Washington, D.C.)*, **104**, 4727 (2004).
17. A. Weber and J. Newman, *Chem. Rev. (Washington, D.C.)*, **104**, 4679 (2004).
18. K. S. Udell, *Int. J. Heat Mass Transfer*, **28**, 485 (1985).
19. M. C. Leverett, *AIME Trans.*, **142**, 152 (1941).
20. J. T. Gostick, M. W. Fowler, M. A. Ioannidis, M. D. Pritzer, Y. M. Volfkovich, and A. Sakars, *J. Power Sources*, **156**, 375 (2006).
21. J. Ohser and F. Mücklich, *Statistical Analysis of Microstructures in Materials Science*, Wiley, Chichester, England (2000).
22. K. Schladitz, S. Peters, D. Reinel-Bitzer, A. Wiegmann, and J. Ohser, *Technical Report No*. 72, Fraunhofer ITWM (2005).
23. R. D. Hazlett, *Transp. Porous Media*, **20**, 21 (1995).
24. M. Hilpert and C. T. Miller, *Adv. Water Resour.*, **24**, 243 (2001).
25. H.-J. Vogel, J. Tölke, V. P. Schulz, M. Krafczyk, and K. Roth, *Vadose Zone J.*, **4**, 380 (2005).
26. P. M. Wilde, M. Mändle, M. Murata, and N. Berg, *Fuel Cells*, **4**, 180 (2004).
27. J. Ihonen, M. Mikkola, and G. Lindbergh, *J. Electrochem. Soc.*, **151**, A1152 (2004).
28. K. Schladitz, S. Peters, D. Reinel-Bitzer, A. Wiegmann, and J. Ohser, *Comput. Mater. Sci.*, **38**, 56 (2006).
29. P. Soille, *Morphological Image Analysis: Principles and Applications*, Springer-Verlag, Berlin (1999).
30. U. Frisch, D. d'Humiéres, B. Hasslacher, P. Lallemand, Y. Pomeau, and J. P. Rivet, *Complex Syst.*, **1**, 649707 (1987).
31. F. J. Higuera, S. Succi, and R. Benzi, *Europhys. Lett.*, **9**, 345 (1989).
32. Y. Qian, D. d'Humiéres, and P. Lallemand, *Europhys. Lett.*, **17**, 479 (1992).
33. I. Ginzburg and D. d'Humiéres, *J. Stat. Phys.*, **84**, 927971 (1996).
34. I. Ginzburg and D. d'Humiéres, *Phys. Rev. E*, **68**, 066614(130) (2003).
35. V. Schulz, D. Kehrwald, A. Wiegmann, and K. Steiner, in *Proceedings of 2nd NAFEMS CFD-Seminar: Flows (CFD) - Application and Trends*, pp. 6.1–6.10, Niedernhausen b. Wiesbaden, Germany, April 25–26, 2005.
36. H.-J. Vogel and K. Roth, *Eur. J. Soil. Sci.*, **49**, 547 (1998).
37. K. R. Mecke, in *Statistical Physics and Spatial Statistics*, K. R. Mecke and D. Stoyan, Editors, pp. 111–184, Springer-Verlag, Berlin (2000).
38. T. Saito and J.-I. Toriwaki, *Pattern Recogn.*, **27**, 1551 (1994).
39. V. P. Schulz, Ph.D. Thesis, Universität Heidelberg (2003).
40. J. Benziger, J. Nehlsen, D. Blackwell, T. Brennean, and J. Itescu, *J. Membr. Sci.*, **261**, 98 (2005).
41. S. Litster, D. Sinton, and N. Djilali, *J. Power Sources*, **154**, 94 (2006).
42. A. Bazylak, D. Sinton, Z.-S. Liu, and N. Djilali, *J. Power Sources*, **163**, 2 (2007).
43. H. Dohle, R. Jung, N. Kimiaie, J. Mergel, and M. Müller, *J. Power Sources*, **124**, 371 (2003).